Supporting Information

Griese et al. 10.1073/pnas.1304368110

SI Results

A Mn^{III}/Fe^{III} Cofactor Prepared Under Aerobic Conditions: EPR Experiments and Spin Hamiltonian Simulations. Solution EPR samples of *Geobacillus kaustophilus* R2lox homolog 1 (*Gk*R2loxI) were prepared under aerobic conditions. Importantly, EPR signals were only observed for *Gk*R2loxI loaded with Mn^{II}, whereas samples reconstituted with only Fe^{II} exhibited no EPR signals. In samples to which only Mn^{II} was added, a protein-bound, monomeric Mn^{II} signal was observed, as described in the main text. In contrast, samples loaded with both Mn^{II} and Fe^{II} under aerobic conditions showed a structured signal centered at $g \approx 2$ using continuous wave (CW) X-band EPR (Fig. 2*A* and Fig. S4). A range of microwave powers (10–100 μW) and magnetic field modulation amplitudes (0.1–1 mT) were used to avoid saturation and spectral artifacts.

A similar structured signal was seen using pulse Q-band EPR (Fig. 2*B*). Spectra were measured using the pulse sequence t_p–τ–$2t_p$–τ–echo, where the length of the π/2 microwave pulse was generally set to $t_p = 12$ ns, and the interpulse distance was varied in the range $\tau = 200$–500 ns. Microwave nutation experiments of the oxidized cofactor, which permit assignment of the multiplicity (spin state) of an EPR-active species, were found to be consistent with a S = 1/2 spin species (discussed in *EPR Theory* below).

The EPR signal of the Mn/Fe cofactor has a *g*-anisotropy that is unusually large for monomeric and dimeric Mn complexes, as inferred from the ≈40-mT increase in the total spectral width between X- and Q-band spectra (Fig. S4). The hyperfine splitting observed (≈10 mT/250 MHz) is similar to that measured for monomeric Mn^{II} and Mn^{IV} ions and for strongly antiferromagnetically exchange-coupled Mn^{II}/Mn^{III} and Mn^{III}/Mn^{IV} complexes (1–3).

The same hyperfine coupling is inferred from ^{55}Mn-electron nuclear double resonance (ENDOR) spectra (Fig. 2*C*). Q-band Davies ENDOR spectra were collected using the pulse sequence t_{inv}–t_{RF}–T–t_p–τ–$2t_p$–τ–echo with the length of the inversion microwave π pulse of $t_{inv} = 16$–24 ns and a radio frequency π pulse length of $t_{RF} = 3.5$ μs. The length of the π/2 microwave pulse in the detection sequence was generally set to $t_p = 8$–12 ns and the interpulse delays to $T = 0.6$ μs and $\tau = 396$ ns.

Further line splitting was observed for the oxidized cofactor when the apoprotein was reconstituted with Mn^{II} and $^{57}Fe^{II}$, confirming that the EPR signal arises from a coupled Mn/Fe spin species (Fig. 2 *A* and *B* and Fig. S4).

^{14}N ligands to the metallocofactor were measured with three-pulse electron spin echo envelope modulation (ESEEM) (Fig. 2*D*), collected using the sequence: t_p–τ–t_p–T–t_p–τ–echo, where the length of the π/2 microwave pulse was set to $t_p = 12$ ns, the interpulse distance (τ) was varied between 200–300 ns and the interpulse distance (*T*) was swept over the range 100–4088 ns with steps $\Delta T = 8$ ns.

Simultaneous simulations of the X- and Q-band EPR spectra are shown in Fig. S4, using the spin Hamiltonian formalism for an S = 1/2 species, i.e., an antiferromagnetically coupled Mn^{III}/Fe^{III} dimer, as described below. The fitted parameters are listed in Table S2. These simulations, which included only one spin system, reproduce the spectral width and all line splittings observed. Our assessment that the EPR signal does arise from only one Mn/Fe cofactor is twofold:

1) The microwave frequency dependence of the cofactor signal in CW and pulse EPR experiments at X- and Q-band demonstrates that if there were two cofactors of appreciable intensity, their *g*-tensors would have to be nearly identical. In Mn dimer model complexes, especially Mn^{II}/Mn^{III} dimers isoelectronic with the Mn^{III}/Fe^{III} cofactor here, the *g*-tensor is sensitive to first coordination sphere changes at both metal sites (3). Thus, it would be surprising if both the correctly metallated (Mn^{III}/Fe^{III}) and mismetallated (Fe^{III}/Mn^{III}) cofactors had the same *g*-tensor.

2) ^{55}Mn-ENDOR spectra (including orientation selective measurements) also show that if there were two cofactors of appreciable intensity, the ^{55}Mn hyperfine (*a*) tensor of both cofactors would have to be near identical, in terms of the isotropic hyperfine (a_{iso}), the hyperfine anisotropy (a_{aniso}), and their orientation relative to the molecular *g*-tensor. Again, in Mn dimer complexes the hyperfine tensor is very sensitive to the coordination sphere of the Mn ion, and indeed even complexes that are virtually identical in terms of first coordination sphere ligands can be readily distinguished using this technique. The best example of this is the set of mixed-valence Mn^{III}/Mn^{IV} model complexes (BIPY, BTNE, TACN, etc.) (2, 4). These complexes have the same bridging ligands (bis-μ-oxo) and basically the same first coordination sphere, all six-coordinate with N/O ligands, but yield different ^{55}Mn-ENDOR spectra. We also note that we can exclude a homodinuclear Mn complex population, as such a cofactor would yield a characteristically broader ^{55}Mn-ENDOR spectrum than experimentally observed.

The fitted spin Hamiltonian parameters were mapped to site (intrinsic) values as described in *EPR Theory* using spin projection coefficients for a Mn^{III}/Fe^{III} cofactor. Here, anisotropic spin projections were used to correctly reproduce the expected onsite hyperfine anisotropy of the Mn^{III} and Fe^{III} (for further details see ref. 5). The spin projection coefficients [ρ_x ρ_y ρ_z] used for the Fe^{III} and Mn^{III} ions, respectively, are Fe^{III} = [2.10, 2.19, 2.73] and Mn^{III} = [−1.10, −1.19, −1.73]. The intrinsic hyperfine tensor components (a_i) are equal to the projected hyperfine tensor components (A_i) divided by the spin projection coefficients ρ_i. The necessity of using anisotropic spin projections suggests that the exchange interaction between the two metal ions falls in the intermediate coupling regime, on the order of $J < |20|$ cm^{-1}. This is no more than 10-fold larger than the expected onsite fine structure (d_i) term of the spin Hamiltonian: For Mn^{III} complexes, *d* is |1| to |5| cm^{-1} (for further details see refs. 5–7). The intrinsic/onsite hyperfine tensors for the Mn^{III} center are similar in magnitude to values previously observed in model Mn^{III} complexes ($A_{iso} = -201$ MHz). It is also noted that the orientation of the Mn^{III} hyperfine tensor relative to the *g*-tensor is completely consistent with Mn model systems that have the same basic ligand field (for further details see ref 5). Thus, the entire EPR dataset of *Gk*R2loxI loaded with Mn^{II} and Fe^{II} under aerobic conditions is consistent with the protein containing a heterobimetallic Mn/Fe cofactor with both metals in the formal +III oxidation state.

EPR Theory. ***The spin Hamiltonian formalism.*** Here we consider a coupled Mn^{III}/Fe^{III} cofactor. A basis set that describes the Mn/Fe spin manifold can be built from the product of the eigenstates of the two interacting spins:

$$|S_1 S_2 M_1 M_2 I_1 I_2 m_1 m_2\rangle. \quad \textbf{[S1]}$$

S_i refers to the electronic spin state (the number of unpaired electrons/spins divided by 2) of each metal ion, M_i refers to

the electronic magnetic sublevel (the different configurations of electrons/spins) of each metal, I_i refers to the nuclear spin state of the metal nucleus (analogous to the electronic state), and m_i refers to the nuclear magnetic sublevel of the metal nucleus. As described in Bencini and Gatteschi (6), M_i takes the values $S_i, S_i - 1, \ldots 1 - S_i, -S_i$ and m_i takes the values $I_i, I_i - 1, \ldots 1 - I_i, -I_i$. Specifically, S_i takes the value 5/2 for Fe^{III} (five unpaired electrons divided by 2) and 2 for Mn^{III}; I_i takes the value 5/2 for ^{55}Mn (100% natural abundance) and 1/2 for ^{57}Fe (relevant for the studies of *Gk*R2loxI reconstituted with ^{57}Fe instead of natural abundance Fe). The spin Hamiltonian that describes the spin manifold of the Mn/Fe system is:

$$\hat{H} = \sum_i \beta_e \vec{B}_0 \cdot \hat{g}_i \cdot \vec{S}_i - \sum_i g_n \beta_n \vec{B}_0 \cdot \vec{I}_i + \sum_i \vec{S}_i \cdot \hat{a}_i \vec{I}_i + \sum_i \vec{S}_i \cdot \hat{d}_i \cdot \vec{S}_i - 2\vec{S}_1 \cdot J \cdot \vec{S}_2 \,. \quad \textbf{[S2]}$$

It contains the four different types of magnetic interactions as well as the electronic coupling terms that need to be considered when interpreting EPR spectra. In order from left to right, these include (*i*) electronic Zeeman term, for the Fe and Mn ion; (*ii*) nuclear Zeeman term, for the ^{55}Mn and ^{57}Fe nucleus; (*iii*) electron-nuclear hyperfine interaction term, for the ^{55}Mn and ^{57}Fe nucleus; (*iv*) fine structure term, for the Mn and Fe ion; and (*v*) electron spin exchange coupling term describing the electronic Mn–Fe interaction.

An effective spin 1/2 ground state. The electronic coupling between the Mn and Fe ions for the oxidized cofactor is sufficiently large that the spin manifold can be treated within the strong exchange limit. Here the two metal ions are strongly interacting such that the unpaired electrons of the Mn and Fe pair with each other, resulting in an effective total spin state of S = 1/2. In this instance, the exchange interaction between the two ions must be significantly larger than any other term of the spin Hamiltonian. The resultant electronic spin states of the manifold are then adequately described by a single quantum number, the total spin (S_T), instead of S_1 and S_2. The "multiline" EPR signal observed for the Mn/Fe complex is derived from only one total spin state, the ground state of the spin manifold with total spin $S_T = 1/2$. For this sublevel all but one electron of the Fe has a partner on the Mn ion, leading to a single unpaired electron, S = 1/2 state. The basis set that describes this subspace takes the form

$$\left| \tfrac{1}{2} \quad M \quad I_1 \quad I_2 \quad m_1 \quad m_2 \right\rangle, \quad \textbf{[S3]}$$

where M takes all half-integer values: $-1/2 \le M \le 1/2$ and I_1, I_2, m_1, and m_2 are as defined above. The effective spin Hamiltonian that describes the ground state of the spin manifold ($S_T = 1/2$) is:

$$\hat{H} = \beta_e \vec{B}_0 \cdot \hat{G} \cdot \vec{S} + \sum_i \left(-g_n \beta_n \vec{B}_0 \cdot I_i + \vec{S} \cdot \hat{A}_i \cdot \vec{I}_i \right). \quad \textbf{[S4]}$$

This simpler spin Hamiltonian now contains only three different types of magnetic interactions: (*i*) electronic Zeeman term, for the total electronic spin; (*ii*) nuclear Zeeman terms, for the ^{55}Mn and ^{57}Fe nucleus; and (*iii*) electron-nuclear hyperfine terms, for the ^{55}Mn and ^{57}Fe nucleus.

Isotropic spin projections. A mapping of the spin subspace, i.e., the S = 1/2 ground state that displays the multiline signal, onto the original basis set can be made using a linear transformation that can be described in terms of spin projections (6, 7). This allows the intrinsic g and hyperfine tensors of the Mn and Fe ions (g_i, a_i, see Eq. **S2**) to be calculated from the effective G and hyperfine tensors (A_i, see Eq. **S4**), allowing the site properties of each metal to be compared with other monomeric/multimeric complexes. For an exchange-coupled Mn^{III}/Fe^{III} complex the effective g-tensor G and hyperfine tensors A_i are related to the parameters of the complete spin Hamiltonian of the exchange-coupled system by the spin projection coefficients given below, where the isotropic spin projection coefficients (ρ_1, ρ_2) are defined as (6, 7):

$$\rho_1(Fe^{III}) = \frac{S_1(S_1+1) - S_2(S_2+1) + S(S+1)}{2S(S+1)}$$
$$\rho_2(Mn^{III}) = \frac{S_2(S_2+1) - S_1(S_1+1) + S(S+1)}{2S(S+1)} \quad \textbf{[S5]}$$

and effective G and hyperfine tensors (A_i), assuming all g_i and a_i are isotropic (6, 7):

$$G = \rho_1 g_1 + \rho_2 g_2 + \frac{\rho_1 \rho_2}{5J}(g_1 - g_2)[(3\rho_1 + 1)d_1 - (3\rho_2 + 1)d_2]$$
$$A_1 = \rho_1 a_1 - a_1 \frac{\rho_1 \rho_2}{5J}[(3\rho_1 + 1)d_1 - (3\rho_2 + 1)d_2] \quad \textbf{[S6]}$$
$$A_2 = \rho_2 a_2 + a_2 \frac{\rho_1 \rho_2}{5J}[(3\rho_1 + 1)d_1 - (3\rho_2 + 1)d_2].$$

For an Fe^{III}/Mn^{III} dimer, $S_1(Fe^{III}) = 5/2$ and $S_2(Mn^{III}) = 2$ gives isotropic spin projection values of $\rho_1 = 7/3$ and $\rho_2 = -4/3$, respectively. In the limit where the exchange coupling J is large, the above relations are approximately $G = 7/3g^{II} + 4/3g^{III}$, $A^{II} = 7/3a^{II}$, $A^{III} = -4/3a^{III}$ (7, 8). Thus, the effective G-tensor is dominated by the onsite g-tensor of the Fe. Similarly, the effective hyperfine coupling of the Mn^{III} ion is scaled up from an onsite value of ~200 MHz to a projected value of 260 MHz (Table S2) (1–3), which must be considered when comparing this value to monomeric Mn^{III} models.

SI Materials and Methods

Cloning, Expression, and Protein Purification. A construct encoding full-length *Geobacillus kaustophilus* R2loxI (accession number yp_148624) was PCR-amplified from genomic DNA (DSM number 7263) and inserted into pET-46 Ek/LIC (Novagen). Expression was carried out in *Escherichia coli* BL21(DE3) (Novagen). Cells were cultured in a bench-top bioreactor system (Harbinger). Metal-bound protein was produced in terrific broth-based autoinduction medium (ForMedium) supplemented with carbenicillin. Cultures were grown at 37 °C for 18 h before harvesting by centrifugation. To obtain apoprotein, cultures were grown at 37 °C in terrific broth (ForMedium) supplemented with carbenicillin. At an optical density (600 nm) of ~1.0, 0.5 mM EDTA was added to the cultures, and expression was induced with 0.5 mM isopropyl β-D-1-thiogalactopyranoside and allowed to continue for 3 h. Metal-bound protein was purified via heat denaturation of contaminating proteins, nickel chelate affinity, and size-exclusion chromatography. Cells from 1.5 L of culture were resuspended in buffer A [25 mM Hepes-Na (pH 7.0), 300 mM NaCl, and 20 mM imidazole] and disrupted by high-pressure homogenization. The lysate was cleared by centrifugation, incubated at 80 °C for 10 min, and again cleared by centrifugation. The supernatant was applied to a Ni-nitrilotriacetic acid (NTA) agarose (Qiagen) gravity flow column. The beads were washed extensively with buffer B (buffer A containing 40 mM imidazole). Protein was then eluted using buffer C (buffer A containing 250 mM imidazole), concentrated, and applied to a size-exclusion column (HiLoad 16/60 Superdex 200 prep grade; GE Healthcare) equilibrated in buffer D [5 mM Hepes-Na (pH 7.0) and 50 mM NaCl]. Fractions containing only *Gk*R2loxI were pooled. Apoprotein was purified similarly. The lysis buffer additionally contained 0.5 mM EDTA. Heat denaturation was performed at 60 °C. The Ni-NTA agarose beads were washed first

with buffer B additionally containing 0.5 mM EDTA followed by buffer B. The eluate from the nickel affinity column was exchanged into buffer E [25 mM Hepes-Na (pH 7.0) and 50 mM NaCl] using a HiTrap Desalting column (GE Healthcare). Purified protein was concentrated to 15–30 mg/mL, aliquoted, flash-frozen in liquid nitrogen, and stored at −80 °C.

Crystallization and Data Collection. *Gk*R2loxI was crystallized by vapor diffusion at 22 °C in 12.5–32.5% (wt/vol) PEG 1500 and 100 mM Hepes-Na (pH 7.0–7.5). Crystals of partially metal-bound protein were additionally soaked in mother liquor containing 5 mM each $FeCl_2$ and $MnCl_2$ for 30 min and then briefly washed in mother liquor supplemented with 15–20% (vol/vol) PEG 400 before flash cooling in liquid nitrogen. Apoprotein crystals were cryoprotected by briefly soaking in 40% (wt/vol) PEG 1500 and 100 mM Hepes-Na (pH 7.0–7.5). To reconstitute the oxidized Mn/Fe cofactor, apoprotein crystals were soaked in mother liquor additionally containing 5 mM each $(NH_4)_2Fe(SO_4)_2$ and $MnCl_2$ for 1–24 h and then briefly washed in cryoprotectant solution. To reconstitute the reduced Mn/Fe cofactor, apoprotein crystals were soaked in 1 mL of cryoprotectant solution additionally containing 5 mM $(NH_4)_2Fe(SO_4)_2$, 5 mM $MnCl_2$, 0.5% (wt/vol) sodium dithionite, 0.5 mM phenosafranin, and 0.05% (vol/vol) Tween 20 for 1–3 h and flash-cooled directly without washing. Data were collected at 100 K at beamlines PX14.1/BESSY, ID23-2/ESRF, and X06SA/SLS. For the purpose of metal quantification, data collection proceeded in the order Fe edge–Mn edge on the same crystal.

Structure Determination, Model Building, and Refinement. Data were processed with XDS (9). The structure of oxidized Mn/Fe-bound *Gk*R2loxI was determined by single-wavelength anomalous dispersion phasing from an Fe peak wavelength dataset. Phases were calculated with Phenix AutoSol (10–13). The model was largely automatically built in Phenix AutoBuild (13–15) and completed by manual building in Coot (16). The structures of *Gk*R2loxI in the reduced Mn/Fe-bound and the metal-free state were solved using the oxidized state structure not containing any ligands as a starting model. Refinement was carried out with phenix.refine (13, 15) and iterated with rebuilding in Coot (16). In the oxidized Mn/Fe-bound state, strong electron density connecting the phenolic oxygen of Tyr162 and the Cβ of Val72 was observed. This ether cross-link was restrained to an ideal distance of 1.45 ± 0.02 Å. Structures were validated using MolProbity (17). Statistics are given in Table S1. All figures were prepared with PyMOL (version 1.4.1; Schrodinger, LLC).

Analysis of Anomalous Diffraction Data. All datasets were integrated over the same resolution range (50.0–3.0 Å) with XDS (9). The Fe and Mn edge datasets from one crystal were placed on a common scale with XSCALE (9). Both scaled and unscaled datasets were analyzed. Anomalous difference maps were calculated with PHENIX (13) using the phases from a ligand-free model. To estimate the relative amounts of Fe and Mn in both metal sites, the intensities of the anomalous difference density peaks in spheres of 1.9 Å radius around the center of the peaks were integrated using Mapman (18). The relative amounts of Fe and Mn in each site can be estimated from the integrated intensities at the Fe and Mn edges when taking into account the different contributions of both elements to the anomalous signal at the two wavelengths if the total occupancy of each site is assumed to be 1, which, according to occupancy refinements, is justified. The quantification results obtained from scaled and unscaled datasets were the same to within 10%, as were results obtained when different models were used for phasing the data.

Sample Preparation for Spectroscopy. To reconstitute the oxidized Mn/Fe cofactor, 200 μM apoprotein were incubated with 2 equivalents of $MnCl_2$ and 1 or 2 equivalents of $(NH_4)_2Fe(SO_4)_2$ in 100 mM Hepes-Na (pH 7.0) and 50 mM NaCl for 1 h at room temperature. Excess metal ions were removed by passing the sample through a HiTrap Desalting column equilibrated in buffer E. The reconstituted protein was concentrated to 0.4–1.4 mM, and 50% glycerol was added before transfer into sample holders and flash cooling in liquid nitrogen. The reduced Mn/Fe cofactor was reconstituted in the same way in an anaerobic tent with the addition of 1 mM sodium dithionite to all buffers. To label the oxidized cofactor with ^{57}Fe, $^{57}FeSO_4$ was used instead of natural abundance $(NH_4)_2Fe(SO_4)_2$. Mn-only loaded *Gk*R2loxI was prepared aerobically using a fourfold molar excess of $MnCl_2$ over apoprotein.

EPR Spectroscopy. EPR spectra were measured at 4.8 K using a Bruker ELEXSYS 500 (X-band) and E580 (Q-band) spectrometer. Experimental settings used were as reported in ref. 5 and in *SI Results*.

Mössbauer Spectroscopy. Mössbauer spectra were recorded on an alternating constant acceleration spectrometer in an Oxford Variox cryostat. The minimum experimental line width was 0.24 mm/s (full width at half maximum). All isomer shifts (δ) are quoted relative to iron metal at 300 K.

Density Functional Theory Calculations. The quantum chemical calculations were performed following a standard cluster approach (19) at the B3LYP*/cc-pvtz(-f) (lacv3p+ for the metals) // B3LYP/lacvp* level of theory (20, 21) (Jaguar, version 7.6; Schrodinger, LLC), including solvation (22), dispersion (23), and zero-point corrections. To investigate the mechanism of cross-link formation a model of the active site complex was constructed from the crystal structure of *Mt*R2lox (PDB ID code 3EE4) (24), including the metal ions, first shell ligands, the cross-link residues V71 (corresponding to V72 in *Gk*R2loxI) and Y162 as well as Y175. The α-carbon and two hydrogen atoms along the backbone of each amino acid were held fixed in the geometry optimizations. The relative binding energies of Mn^{II} and Fe^{II} to two different reduced structures were investigated: the heterodinuclear Mn/Fe *Gk*R2loxI (this study), and the homodinuclear Fe/Fe class Ia *E. coli* R2 (PDB ID code 1XIK) (25). The metals, first shell ligands, and the radical-bearing tyrosine in R2 or corresponding phenylalanine in R2lox were included in the models of the active sites. For R2lox the negatively charged fatty acid ligand was also included. The solvated metal ions were modeled as M^{II} ions coordinated with six waters in a continuum water solvent.

Mass Spectrometry. Twenty micrograms of metal-bound *Gk*R2loxI were subjected to proteolytic digestion by Glu-C (Promega) in phosphate buffer (following the manufacturer's instructions). In these conditions, the protein is cleaved at the C-terminal side of glutamic and aspartic acid residues. The digested sample was then dissolved in 100 μL of solvent A (see below). The auto sampler of a HPLC 1200 system (Agilent Technologies) injected 0.5 μL (100 ng of peptides) into a C18 guard desalting column (Zorbax 300SB-C18, 5 × 0.3 mm, 5-μm bead size; Agilent). A 15-cm-long C18 picofrit column (100-μm internal diameter, 5-μm bead size; Nikkyo Technos) installed on to the nano electrospray ionization source was then used. Solvent A was 97% water, 3% acetonitrile (ACN), and 0.1% formic acid (FA); solvent B was 5% water, 95% ACN, and 0.1% FA. At a constant flow of 0.4 μL/min, a linear gradient went from 2% B up to 40% B in 45 min, followed by a steep increase to 100% B in 5 min. Online liquid chromatography-MS was performed using a Q-Exactive mass spectrometer (Thermo Scientific). Fourier transform MS master scans (AGC target of 1e6) were acquired with a resolution of 70,000 and were followed by data-dependent MS/MS (AGC target of 1e5) at a resolution of 17,500. In d-d MS/MS, the top five ions from the master scan were selected for higher energy collision dissociation (at 30% energy). Precursors were isolated with a 2 *m/z* window. Dynamic exclusion was used with 60-s duration.

1. Randall DW, et al. (1995) 55Mn ESE-ENDOR of a mixed-valence Mn(III)Mn(IV) complex - comparison with the Mn cluster of the photosynthetic oxygen-evolving complex. *J Am Chem Soc* 117(47):11780–11789.
2. Schafer KO, et al. (1998) Electronic structure of antiferromagnetically coupled dinuclear manganese ((MnMnIV)-Mn-III) complexes studied by magnetic resonance techniques. *J Am Chem Soc* 120(50):13104–13120.
3. Teutloff C, et al. (2005) High-field EPR investigations of Mn(III)Mn(IV) and Mn(II)Mn (III) states of dimanganese catalase and related model systems. *Magn Reson Chem* 43(Spec no):S51–S64.
4. Schafer KO (2002) Exchange coupled manganese complexes: model systems for the active centres of redoxproteins investigated with EPR techniques. (Technische Univ Berlin, Berlin).
5. Cox N, et al. (2011) Electronic structure of a weakly antiferromagnetically coupled Mn (II)Mn(III) model relevant to manganese proteins: A combined EPR, 55Mn-ENDOR, and DFT study. *Inorg Chem* 50(17):8238–8251.
6. Bencini A, Gatteschi D (1990) *EPR of Exchange Couple Systems* (Springer, Berlin).
7. Sage JT, et al. (1989) Moessbauer analysis of the binuclear iron site in purple acid phosphatase from pig allantoic fluid. *J Am Chem Soc* 111(18):7239–7247.
8. Kulik LV, Epel B, Lubitz W, Messinger J (2007) Electronic structure of the Mn_4O_xCa cluster in the S_0 and S_2 states of the oxygen-evolving complex of photosystem II based on pulse ^{55}Mn-ENDOR and EPR spectroscopy. *J Am Chem Soc* 129(44):13421–13435.
9. Kabsch W (2010) Xds. *Acta Crystallogr D Biol Crystallogr* 66(Pt 2):125–132.
10. Grosse-Kunstleve RW, Adams PD (2003) Substructure search procedures for macromolecular structures. *Acta Crystallogr D Biol Crystallogr* 59(Pt 11):1966–1973.
11. McCoy AJ, et al. (2007) Phaser crystallographic software. *J Appl Cryst* 40(Pt 4):658–674.
12. Terwilliger TC, et al. (2009) Decision-making in structure solution using Bayesian estimates of map quality: The PHENIX AutoSol wizard. *Acta Crystallogr D Biol Crystallogr* 65(Pt 6):582–601.
13. Adams PD, et al. (2010) PHENIX: A comprehensive Python-based system for macromolecular structure solution. *Acta Crystallogr D Biol Crystallogr* 66(Pt 2):213–221.
14. Terwilliger TC, et al. (2008) Iterative model building, structure refinement and density modification with the PHENIX AutoBuild wizard. *Acta Crystallogr D Biol Crystallogr* 64(Pt 1):61–69.
15. Afonine PV, et al. (2012) Towards automated crystallographic structure refinement with phenix.refine. *Acta Crystallogr D Biol Crystallogr* 68(Pt 4):352–367.
16. Emsley P, Lohkamp B, Scott WG, Cowtan K (2010) Features and development of Coot. *Acta Crystallogr D Biol Crystallogr* 66(Pt 4):486–501.
17. Chen VB, et al. (2010) MolProbity: All-atom structure validation for macromolecular crystallography. *Acta Crystallogr D Biol Crystallogr* 66(Pt 1):12–21.
18. Kleywegt GJ, Jones TA (1996) xdlMAPMAN and xdlDATAMAN - programs for reformatting, analysis and manipulation of biomacromolecular electron-density maps and reflection data sets. *Acta Crystallogr D Biol Crystallogr* 52(Pt 4):826–828.
19. Roos K, Siegbahn PEM (2011) Oxygen cleavage with manganese and iron in ribonucleotide reductase from *Chlamydia trachomatis*. *J Biol Inorg Chem* 16(4):553–565.
20. Frisch MJ, et al. (2004) *Gaussian 03, Revision D.01* (Gaussian, Inc., Wallingford, CT).
21. Reiher M, Salomon O, Artur Hess B (2001) Reparameterization of hybrid functionals based on energy differences of states of different multiplicity. *Theor Chem Acc* 107 (1):48–55.
22. Blomberg MRA, Siegbahn PEM, Babcock GT (1998) Modeling electron transfer in biochemistry: A quantum chemical study of charge separation in *Rhodobacter sphaeroides* and Photosystem II. *J Am Chem Soc* 120(34):8812–8824.
23. Grimme S (2006) Semiempirical GGA-type density functional constructed with a long-range dispersion correction. *J Comput Chem* 27(15):1787–1799.
24. Andersson CS, Högbom M (2009) A *Mycobacterium tuberculosis* ligand-binding Mn/Fe protein reveals a new cofactor in a remodeled R2-protein scaffold. *Proc Natl Acad Sci USA* 106(14):5633–5638.
25. Logan DT, et al. (1996) Crystal structure of reduced protein R2 of ribonucleotide reductase: The structural basis for oxygen activation at a dinuclear iron site. *Structure* 4(9):1053–1064.

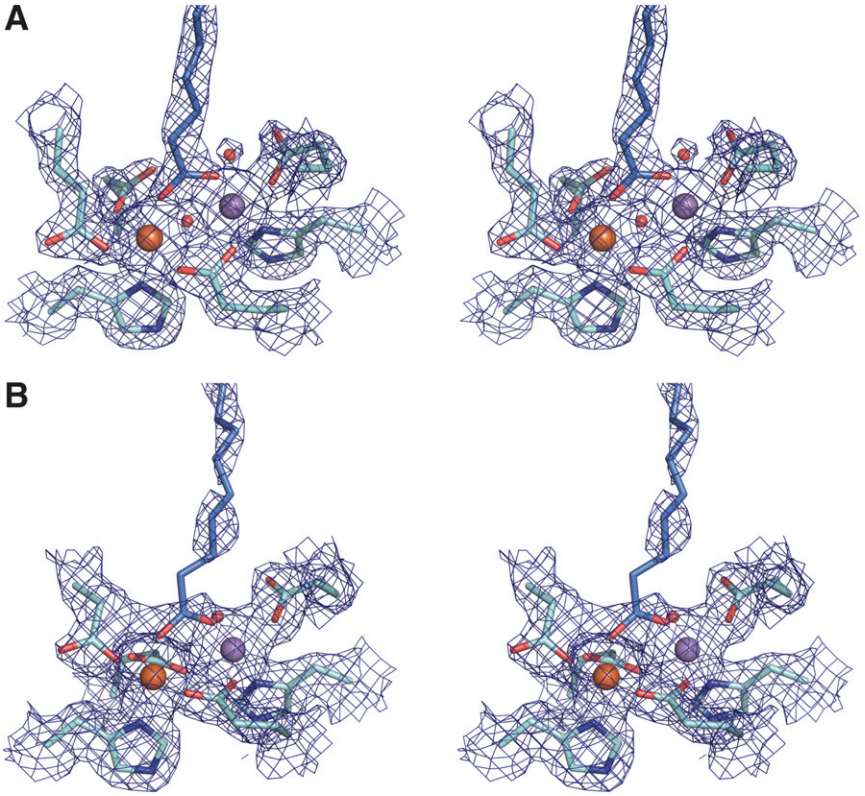

Fig. S1. Stereoview of the $2mF_o$-DF_c electron density around the active site of *Gk*R2loxI in (*A*) the oxidized Mn/Fe-bound state, contoured at 2 σ, and (*B*) the reduced Mn/Fe-bound state, contoured at 1.5 σ. Shown are the metal ions (orange sphere, iron; purple sphere, manganese), coordinating amino acid residues (cyan), water ligands (red spheres), and the fatty acid ligand (blue).

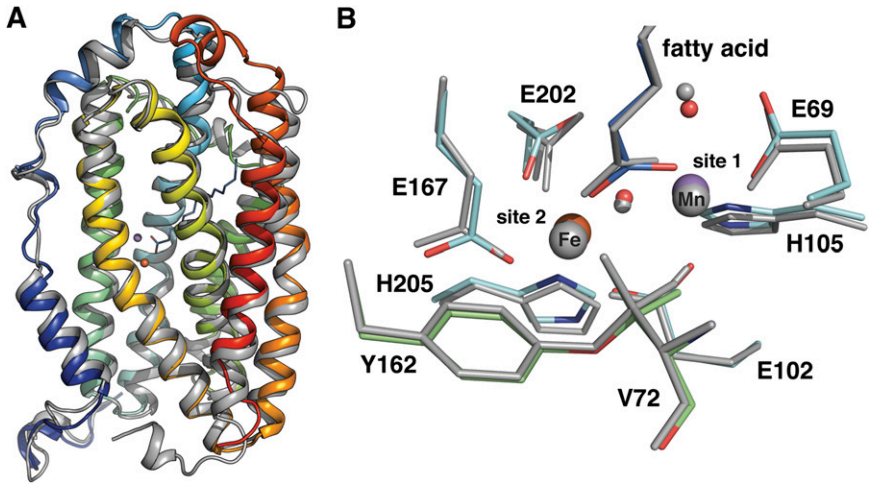

Fig. S2. Comparison of *Gk*R2loxI and *Mt*R2lox. (*A*) Superposition of the *Gk*R2loxI protomer in the oxidized Mn/Fe-bound state (chainbow coloring) with the *Mt*R2lox protomer (gray, PDB ID code 3EE4) (24). The metal ions in *Gk*R2loxI are depicted as spheres (orange, iron; purple, manganese), and the fatty acid ligand is shown as stick model (blue). Ligands in *Mt*R2lox are not shown. (*B*) Superposition of the oxidized Mn/Fe-bound active sites of *Gk*R2loxI (cyan, metal-coordinating residues; green, cross-linked residues; blue, fatty acid) and *Mt*R2lox (gray). Residue numbering is for *Gk*R2loxI.

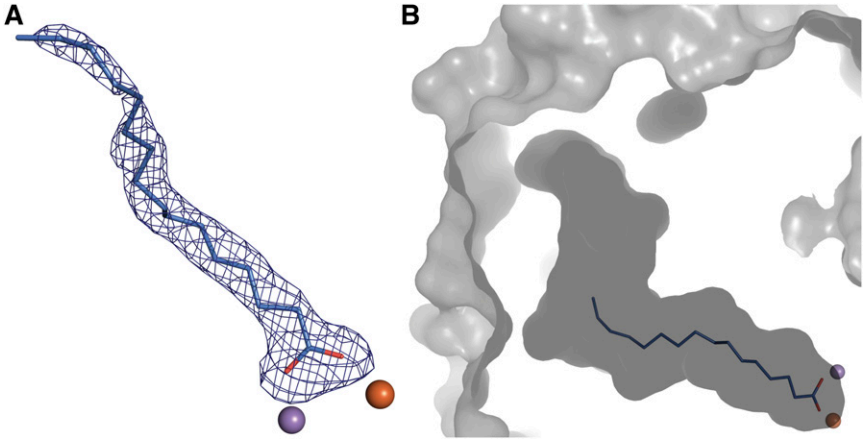

Fig. S3. A long-chain fatty acid is bound in the active site of *Gk*R2loxI. (*A*) mF_o-DF_c omit electron density for the copurified ligand bound in the oxidized Mn/Fe-bound active site, contoured at 3 σ. The ligand is best modeled as palmitic acid, but the electron density is less well defined as the cavity becomes wider toward the protein surface. It may therefore in fact be a mixture of different long-chain fatty acids. (*B*) The ligand-binding pocket. The molecular surface volume of the pocket is 1,037 $Å^3$ as calculated by CASTp (1) using a 1.4-Å probe radius.

1. Dundas J, et al. (2006) CASTp: Computed atlas of surface topography of proteins with structural and topographical mapping of functionally annotated residues. *Nucleic Acids Res* 34(Web Server issue):W116–W118.

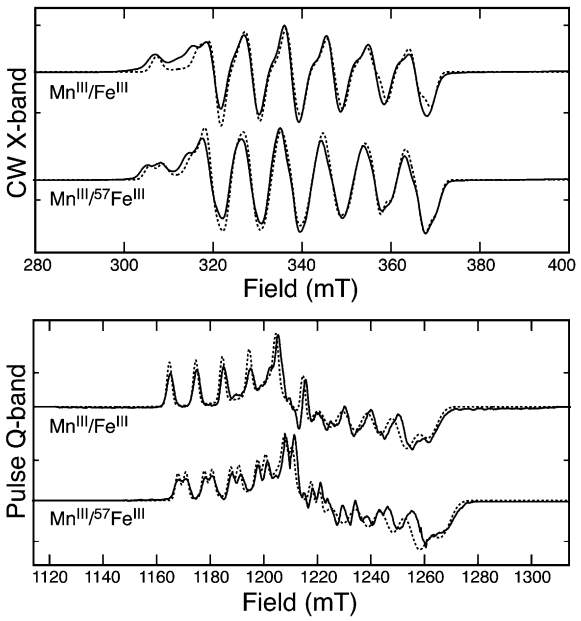

Fig. S4. Multifrequency EPR spectra of the Mn^{III}/Fe^{III} cofactor. The dashed lines represent a least-squares fitting to the whole dataset using a model based on the spin Hamiltonian formalism. The optimized parameter sets are given in Table S2.

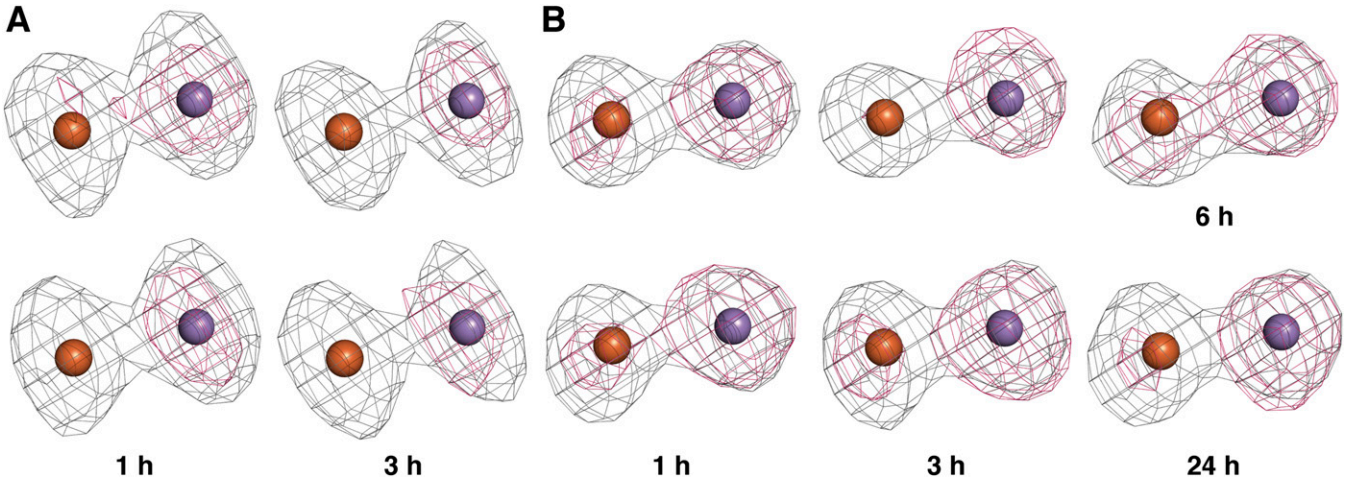

Fig. S5. Anomalous difference density around the metal-binding sites at the Fe (gray) and Mn (pink) edges from apoprotein crystals soaked with Mn^{II} and Fe^{II} under (*A*) anoxic (in the presence of 0.5% sodium dithionite) or (*B*) aerobic conditions (in air-saturated buffer) for the durations indicated below each panel. Maps are contoured at four electrons per cubic angstrom. For clarity, the metal ions are depicted as Fe in site 2 (orange sphere) and Mn in site 1 (purple sphere). For 1-h and 3-h soaking duration, data were collected from two crystals each.

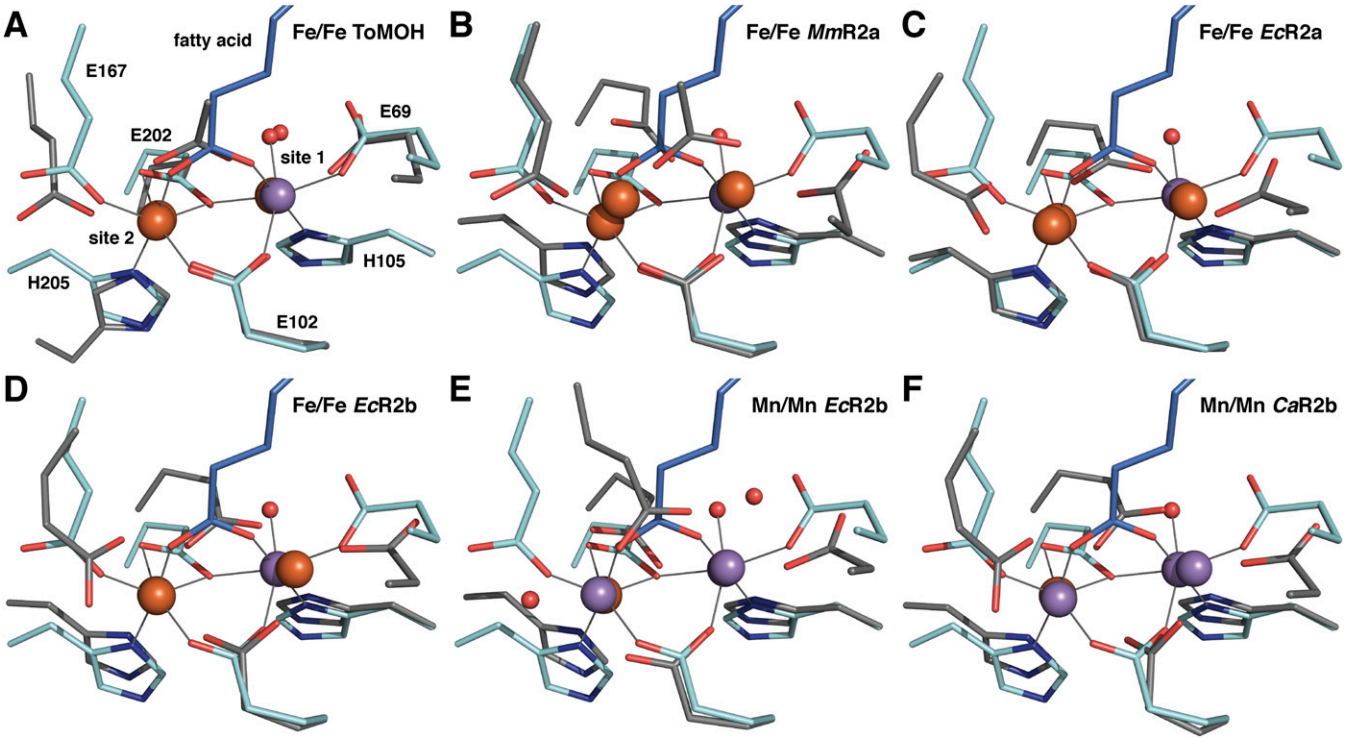

Fig. S6. Differences and similarities between the reduced metal-bound active sites of *Gk*R2loxI and other ferritin-like proteins with different metal specificities. Residues 102–105 of *Gk*R2loxI were superimposed with the corresponding residues of (*A*) reduced Fe/Fe-bound *Pseudomonas mendocina* toluene 4-monooxygenase hydroxylase with an acetate ligand (ToMOH, PDB ID code 3DHI) (1), (*B*) reduced Fe/Fe-bound mouse class Ia R2 protein with an acetate ligand (*Mm*R2a, PDB ID code 3W69) (2), (*C*) reduced Fe/Fe-bound *E. coli* class Ia R2 protein (*Ec*R2a, PDB ID code 1XIK) (3), (*D*) reduced Fe/Fe-bound *E. coli* class Ib R2 protein (*Ec*R2b, PDB ID code 3N38) (4), (*E*) reduced Mn/Mn-bound *E. coli* class Ib R2 protein (PDB ID code 3N37) (4), and (*F*) reduced Mn/Mn-bound *Corynebacterium ammoniagenes* class Ib R2 protein (*Ca*R2b, PDB ID code 1KGP) (5). The metal-coordinating residues of *Gk*R2loxI are shown in cyan, the fatty acid ligand in blue, and all superimposed structures in gray; residue numbering in *A* is for *Gk*R2loxI.

1. Bailey LJ, McCoy JG, Phillips GN, Jr., Fox BG (2008) Structural consequences of effector protein complex formation in a diiron hydroxylase. *Proc Natl Acad Sci USA* 105(49):19194–19198.
2. Strand KR, et al. (2004) Crystal structural studies of changes in the native dinuclear iron center of ribonucleotide reductase protein R2 from mouse. *J Biol Chem* 279(45):46794–46801.
3. Logan DT, et al. (1996) Crystal structure of reduced protein R2 of ribonucleotide reductase: the structural basis for oxygen activation at a dinuclear iron site. *Structure* 4(9):1053–1064.
4. Boal AK, Cotruvo JA, Jr., Stubbe J, Rosenzweig AC (2010) Structural basis for activation of class Ib ribonucleotide reductase. *Science* 329(5998):1526–1530.
5. Högbom M, Huque Y, Sjöberg BM, Nordlund P (2002) Crystal structure of the di-iron/radical protein of ribonucleotide reductase from *Corynebacterium ammoniagenes*. *Biochemistry* 41(4):1381–1389.

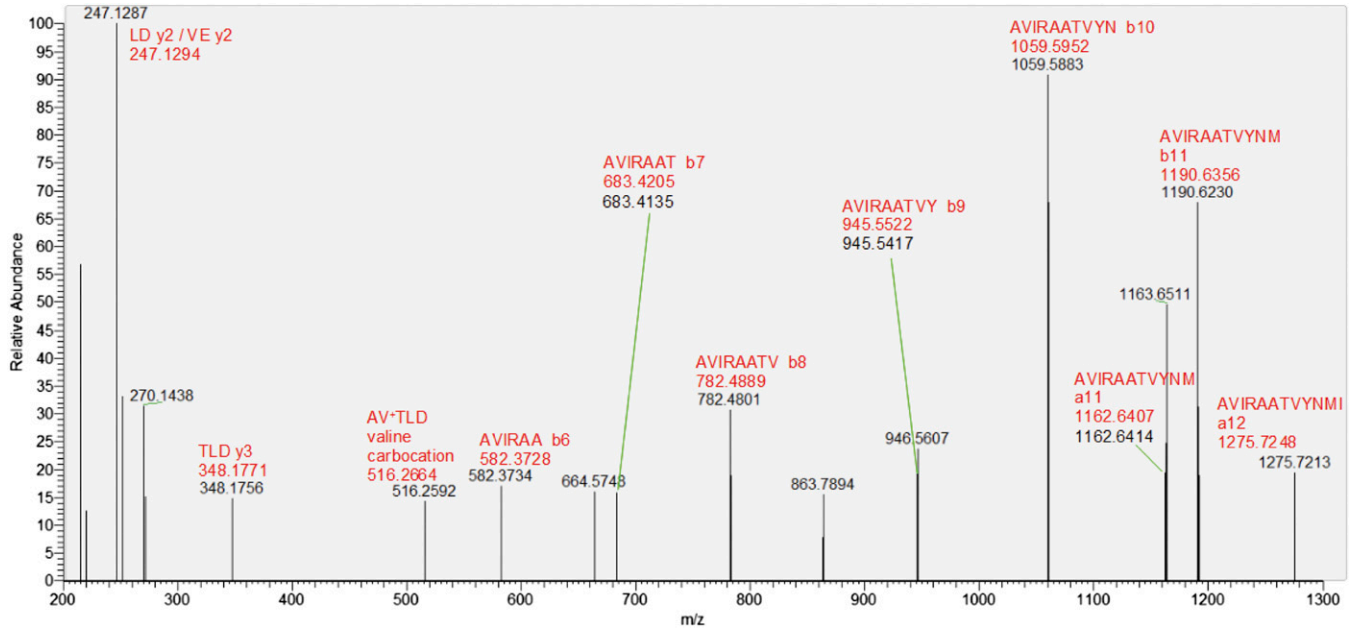

Fig. S7. Annotated MS/MS spectrum of the triply charged precursor ion 689.0381 *m/z*, which corresponds to the tyrosine–valine ether–cross-linked peptide AVIRAATVYNMIVE-AVTLD, obtained by proteolytic digestion of metal-bound *Gk*R2loxI with Glu-C. The experimental *m/z* values are in black, whereas the annotation and theoretical *m/z* values are shown in red. The mass error is typically less than 0.01 *m/z*, in accordance with the high resolution used (17,500). Among the fragment ions observed, a series of b ions from the AVIRAATVYNMIVE sequence can be found, as well as y ions from the AVTLD sequence. Most importantly, the $AV^{+}TLD$ valine carbocation can only be explained by cleavage (induced by higher-energy collisional dissociation fragmentation) at the ether cross-link.

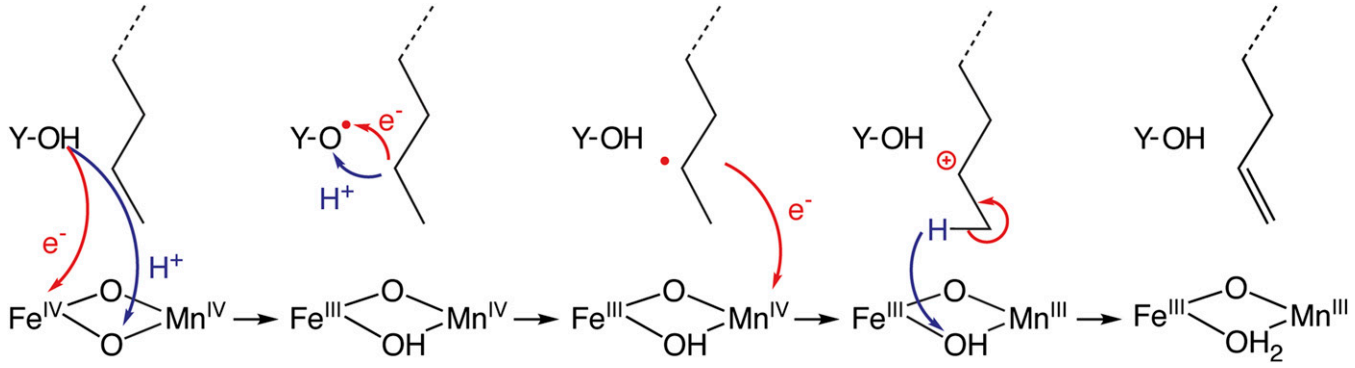

Fig. S8. Reaction scheme of a hypothetical desaturation reaction catalyzed by the heterodinuclear Mn/Fe-*Gk*R2loxI. In analogy to the investigated mechanism of cross-link formation, the desaturation mechanism involves the formation of a Y175 radical coupled to reduction of Fe^{IV}. The radical is transferred, by hydrogen atom transfer, from Y175 to the substrate. An electron transfer from the substrate radical to the metal center leads to the formation of a substrate carbocation. In the final step the substrate is deprotonated and desaturated. The formation of the Y175 radical is exothermic. An estimate of the relative stability of the secondary radical and cation of the substrate compared with the tertiary radical and cation of valine is lower by 3.3 and 13.8 kcal/mol, based on small models of hexane and isobutene. Adding these numbers to the corresponding states in the energy profile for the link formation gives an estimate for a rate-limiting radical transfer from Y175 to the substrate of ~17–18 kcal/mol, a reasonable barrier.

Table S1. Data collection, phasing, and refinement statistics

Table S1

Values in parentheses are for the highest resolution shell. For native datasets, Friedel pairs were merged.
*The protein was produced and purified in partially metal-bound form, and crystals were additionally soaked with Mn^{II} and Fe^{II} under aerobic conditions for 30 min.
†The protein was produced and purified in metal-free (apo) form, and crystals were soaked with Mn^{II} and Fe^{II} for the indicated durations under reducing anoxic (red; in the presence of 0.5% sodium dithionite) or oxidizing aerobic (ox; in air-saturated buffer) conditions.
‡The protein was produced and purified in metal-free (apo) form.
§R_{free} is calculated from a randomly selected 5% subset of reflections excluded from refinement.
¶Residues out of the 302 residue full-length protein included in the final model are given in parentheses.
‖Geometry statistics were calculated with MolProbity (1).
**Average *B* factors were calculated with Baverage in the CCP4 suite (2).

1. Chen VB, et al. (2010) MolProbity: All-atom structure validation for macromolecular crystallography. *Acta Crystallogr D Biol Crystallogr* 66(Pt 1):12–21.
2. Winn MD, et al. (2011) Overview of the CCP4 suite and current developments. *Acta Crystallogr D Biol Crystallogr* 67(Pt 4):235–242.

Table S2. Principal values of the effective *g*, ^{55}Mn, and ^{57}Fe hyperfine tensors for the spin Hamiltonian simulations of the oxidized Mn^{III}/Fe^{III} cofactor

Table S2

The isotropic g_{iso} and A_{iso} values are the average of the individual values: $g_{iso} = (g_x + g_y + g_z)/3$ and $A_{iso} = (A_x + A_y + A_z)/3$. The anisotropy in the g and A_i values is expressed as the difference between the parallel and perpendicular component of the tensor. The intrinsic hyperfine tensor components (a_i) are equal to the projected hyperfine tensor components (A_i) divided by the spin projection coefficients ρ_i as defined in *EPR Theory*. The spin projection coefficients [ρ_x ρ_y ρ_z] for the Fe^{III} and Mn^{III} ion are Fe^{III} = [2.10, 2.19, 2.73] and Mn^{III} = [−1.10, −1.19, −1.73].